7th Quarter Research Performance Progress Report

Project Title:	Pore Scale Control of Gas and Fluid Transport at Shale Matrix-Fracture Interfaces
Project Period:	10/01/16 – 09/30/18
Reporting Period:	4/1/18 – 6/30/18
Submission Date:	7/30/2018
Recipient:	SLAC National Accelerator Laboratory
Recipient DUNS #:	00-921-4214
Address:	2575 Sand Hill Road, MS 69 Menlo Park, CA 94025
Website (if available)	www-ssrl.slac.stanford.edu
Award Number:	FWP 100211
Awarding Agency:	NETL

Principal Investigator: Dr. John Bargar
Senior Staff Scientist
SLAC National Accelerator Laboratory
Phone: 650-926-4949
Email: bargar@slac.stanford.edu

Co-Principal Investigators: Dr. Gordon E. Brown, Jr.
Dr. Kate Maher
Dr. Anthony Kovscek
Dr. Mark Zoback

NETL Project Manager: David Cercone

TABLE OF CONTENTS

1. .... GOALS AND OBJECTIVES 3
2. ....TECHNICAL HIGHLIGHTS 4
3. .... RESULTS AND DISCUSSION: TASK 2 5
4... RESULTS AND DISCUSSION: TASK 3&4a 6
5... RESULTS AND DISCUSSION: TASK 3&4b 9
6...RESULTS AND DISCUSSION: TASK 3&4c 13
7……………………………………………………………………MISCELLANEOUS 20
8………………………………………………………………………REFERENCES 21
9...RISK ANALYSIS 21
10. ....MILESTONE STATUS 22
11. ....SCHEDULE STATUS 24
12. .... COST STATUS 26
13… .... COLLABORATIVE LEVERAGING 27
14.. CONCLUSIONS 27
APPENDIX A ....DELIVERABLES 28

1. GOALS AND OBJECTIVES

Shale reservoirs are highly complex physically and chemically. The majority of chemical additives used in hydraulic fracturing were developed based on research findings from conventional oil/gas systems. Due to the difference in industrial processes and source material, a different way of thinking for unconventional systems is needed. As a community, we lack understanding of the fundamental geochemical and kinetic parameters that govern precipitation of ubiquitous scale phases such as barite in unconventional reservoirs during and following stimulation. We also lack basic physical-chemical numerical models to predict gas and fluid transport across the altered zone.

This project is conducting fundamental research to address two crucial and interrelated reservoir performance needs that provide the potential to deliver significant increases in efficiency:

(i) Reducing scale precipitation through better understanding and control of fundamental geochemical and kinetic factors; and

(ii) Improving microscale knowledge of the fracture-matrix interface required to develop chemical/physical manipulation approaches that can access resource in the matrix.

We are accomplishing these goals through a suite of activities that integrate synchrotron-based imaging and CT methods, electron microscopy, permeability measurements, and geochemical and reactive transport modeling. This approach is allowing us to associate pore- and fracture-scale geochemical processes to resultant changes in transport properties.

Task 1 encompasses project management activities. The three scientific tasks defined in our project management plan are (**Figure 1**): **Task 2**: Characterizing the influence of dissolved organic compounds, pH, and ionic strength on barite scale precipitation. In contrast, **Tasks 3 and 4** are focused on characterizing and modeling the chemical/microstructural alteration of shale-fracture interfaces and the impact of this alteration on gas transport. **Task 3** is nominally oriented toward porosity generation within the altered layer, whereas **Task 4** is focused on secondary mineral precipitation within the altered layer (‘precipitation favorable’ conditions). These two chemical processes are interrelated (dissolution leads to precipitation), and the work flows for subtasks 3 and 4 are similar. Consequently, Task 3 and 4 efforts have been merged and are reported in section 3 (this section) as “**Task 3&4**”. The merged work flow for **Task 3&4** self-organizes into 3 primary activities: (a) Chemical reactions and sub-core-scale geochemical characterization; (b) permeability measurement, which requires whole-core characterization using core-flood approaches; and (c) numerical modeling of altered shale-matrix interfaces. Results for each are presented separately later in this section. Effort for **Task 3&4** in Year 1 has focused on activities (a) and (b), whereas numerical modeling will be a more significant focus in Year 2.

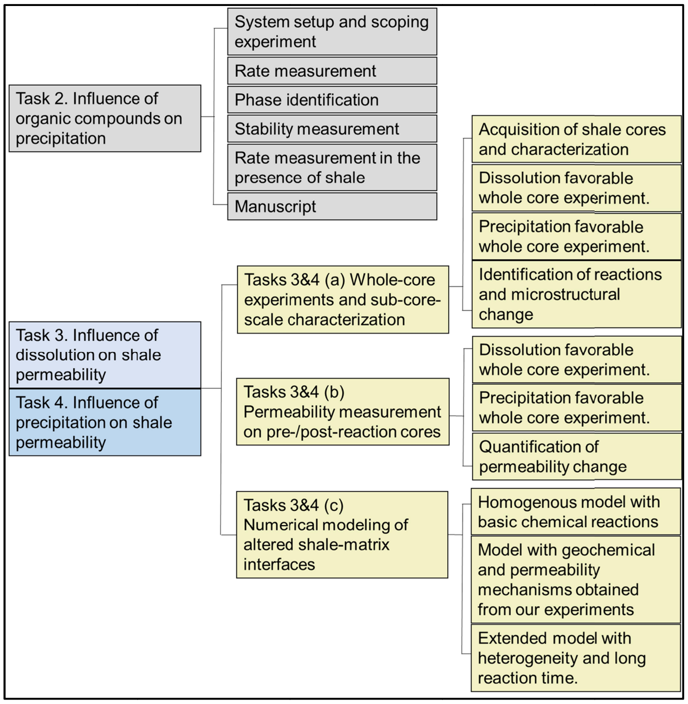

Figure 1. Structure of this report and the relation to PMP tasks. Task 1 (not illustrated) is the program management activity.

2. TECHNICAL HIGHLIGHTS

Task-by-task highlights of accomplishments in Quarter 7:

Task 1

1. The approved project management plan is being implemented with each goal being completed on-time.
2. Teleconference and in-person meetings with research scientists at NETL are conducted as needed.

Task 2

3. The manuscript associated with this task has been submitted to Energy & Fuels for review and potential publication.

Tasks 3 & 4 (a) Fundamental precipitation and dissolution reactions controlling porosity

4. SEM images were collected from cross sections of reacted shales and analyzed to observe secondary porosity. X-ray microprobe images were re-analyzed to support the results of the SEM imaging.

Tasks 3 & 4 (b) Measuring permeability alteration induced by fracture fluid reaction

5. Micro CT Imaging and segmentation were collected on both post-reaction Marcellus and Eagle Ford samples to identify the depth of the penetration from the reaction fluid front into the altered zone.
6. Porosity calculation from fluid penetration porosimetry measurements on both pre- and post-reaction Marcellus and Eagle Ford samples

Tasks 3 & 4 (c) Numerical simulation of secondary porosity generation and scale precipitation during shale-fluid interactions

7. Kinetic/thermodynamic modeling of shale experiments to develop a chemical reaction network for shale-fluid interactions.
8. A one-dimensional reactive transport model was developed to simulate whole core experiments under dissolution-favorable conditions in order to understand the coupling between chemical reactions and transport during shale-fluid interactions.

Details of task progress:

Task 2: Effects of dissolved organic matter on the precipitation and stability of secondary mineral phases

Barite ($BaSO_4$) scale precipitation is a prime concern in nearly all hydraulic fracturing systems, both in shale bodies and in piping, because of its ubiquitous presence and low solubility, tends to be over-saturated. Barite is added to drilling muds (DM) at high concentrations (> 10 g/kg) in order to increase the density of the muds and aid in the drilling process [1-3]. Even though some operators attempt to remove as much of the drilling mud as possible, significant amounts of DM is imbedded in the rock during the drilling process remain. This leftover DM can then react with the initial hydrochloric acid slug (~15%) injected down bore hole to clean up perforations in the bore casing and to help clean out the drilling mud. In comparison to the drilling mud, barium concentrations native to the shale host rock are lower, typically ≤ 1 g/kg in the solid [4]. The high volume/pressure of the injection fluid and the low pH (~ pH 0), result in a high probability of dissolving and mobilizing Ba from the DM and forcing it into the natural fractures as well as the shale matrix itself. This introduction of significant quantities of Ba^{2+} and SO_4^{2-}, including that which is leached from the shale itself, will lead to scale production, clogging of newly developed secondary porosity, and overall attenuation of permeability.

The scope of this task includes investigating the effects of various classes of added and natural organics found in hydraulic fracturing systems, including fracture fluid additives (biocides, breakers, crosslinkers, friction reducers, scale inhibitor, Fe-control, corrosion inhibitor, and gellants), as well as those present in shale (both formation and produced waters). Major questions being addressed by this task are, how do variations in pH, ionic strength, dissolved organic compounds, and mineral surface area impact Ba release into hydraulic fracturing systems and subsequent barite scale precipitation?

Progress in quarter 7:

A draft of the manuscript has been submitted to Energy & Fuels for review

Results and Planned Experiments: All planned experimental work for this task is complete.

Table 1: Task 2 objectives for Quarter 7

Goal	Status
Initial draft of manuscript	Completed
Manuscript submission	Completed

Manuscript plans: A manuscript draft detailing the effect of various organics on the precipitation of barite at various ionic strengths has been submitted to Energy & Fuels for review and potential publication. The manuscript includes variations, the lack of variation in speciation and crystallinity of Ba-bearing precipitates. A working title for this manuscript is: Organic and inorganic controls on barite precipitation in hydraulic fracturing systems. Additionally, a peer-reviewed extended abstract (conference paper) was accepted and published for the URTeC conference this summer in Houston, TX entitled: Barium Sources in Hydraulic Fracturing Systems and Chemical Controls on its Release into Solution.

Task 3&4 (a): Fundamental precipitation and dissolution reactions controlling porosity

Understanding the properties of the altered zone at shale surfaces through experimentation and modeling is centrally important to developing chemical manipulation technologies to increase the efficiency and recovery factors for unconventional gas and oil production. Our ultimate goal is to manipulate the permeability of the altered zone *in-formation* to increase access to matrix. To do this successfully, we need to understand how to induce the formation of connected porosity across the altered zone without triggering geochemical reactions that precipitate secondary minerals. In the present quarter, we present important new results that help to constrain two seminal properties of the altered zone, *thickness* (**Task 3&4(a)**) and *permeability* (**Task 3&4 (b)**). In **Task 3 & 4 (c)**, secondary porosity generation and mineral precipitation is numerically simulated in order to understand the mechanisms of shale-fluid interactions and predict future shale alteration based on initial shale mineralogy.

In this section (**Task 3&4(a)**) we reacted whole cores with fracture fluid and characterized them with μ-x-ray CT and synchrotron μ-XRF chemical mapping to determine porosity changes, alteration zone thickness, primary minerals dissolving (e.g., carbonate and pyrite), and precipitating phases (e.g., Fe/Al oxides and Ca/Ba sulfate). These measurements allow us to identify the spatial distribution of these reactions within the shale pore structure.

Table 2: Objectives in Tasks 3&4 (a) for Quarter 7.

Goal	Status
Observe secondary porosity in shale matrix using SEM imaging	Complete

Progress in Quarter 7:

Results from prior quarters quantified the reaction depths of S oxidation, Fe oxidation and precipitation, and barite precipitation. However, the secondary porosity created by carbonate dissolution was hard to observe from μ-CT and μ-XRF microprobe. In Quarter 7, we successfully observed secondary porosity from SEM imaging using backscattered electron (BSE) mode.

Results in Quarter 7:

To observe secondary porosity in shale matrices, cross sections from post-reaction Pennsylvania Marcellus (Marcellus-PA) and Eagle Ford cores were polished to a roughness of 1 μm. The polishing quality allows for SEM imaging using backscattered electron (BSE) mode. Under reaction Condition 1 the shale core was reacted with synthetic fracture fluid, whereas under reaction Condition 2, additional Ba^{2+} and SO_4^{2-} were added to the fracture fluid to promote barite precipitation.

Marcellus-PA cross section images are shown in **Figure 2**. For both reaction conditions, dissolution fronts are hard to observe because of the low percentage (1%) of carbonate. Secondary porosity observed on the images for both conditions is due to dissolution of carbonate grains.

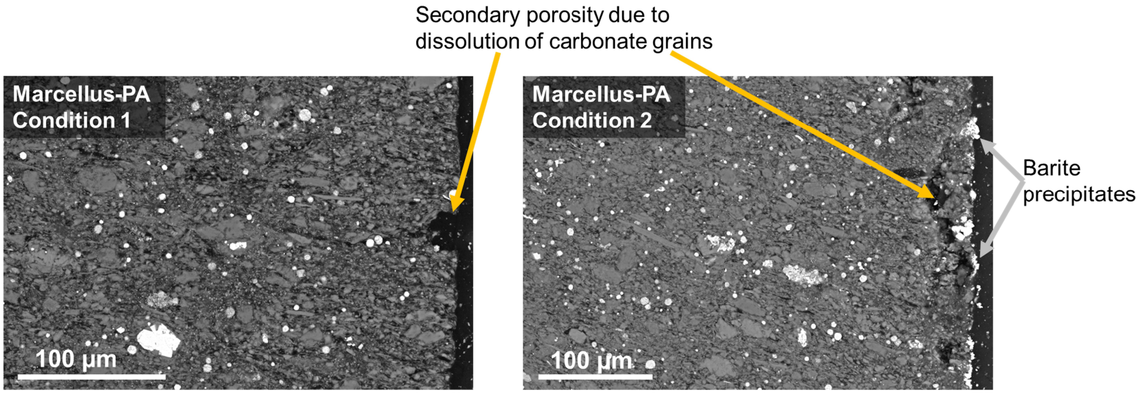

Figure 2. SEM-BSE images of cross sections from post-reaction Marcellus-PA cores. Condition 1 refers to reactions in fracture fluid, and Condition 2 refers to reactions in fracture fluid with additional Ba^{2+} and SO_4^{2-} to form barite scale. Observable secondary pores are created from dissolution of local carbonate grains.

Because it is difficult to quantify the depths of carbonate dissolution from SEM-BSE images, re-analysis of synchrotron μ-XRF mapping collected at SSRL beamline 2-3 was conducted. The cross-section maps were collected with x-ray energies optimized for observation of Fe species, The fluorescence signal from Ca atoms was simultaneously recorded to image the reaction front. As $CaCO_3$ is dissolved, less Ca is present, and the Ca signal decreases. We can thus use the Ca signal to quantify the depth of penetration of acid and carbonate dissolution. **Figure 3** shows that the dissolution fronts for both conditions extend 70 – 150 μm from the shale-fluid interface into the shale matrix.

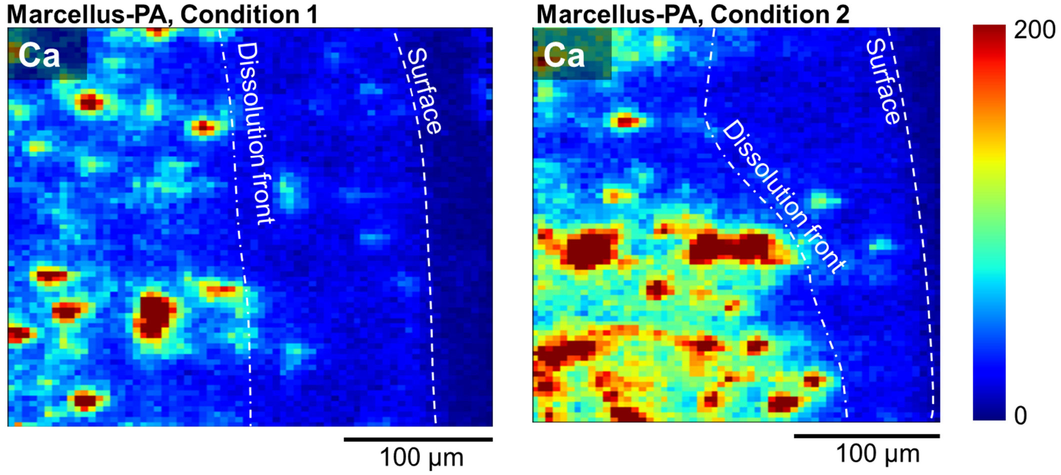

Figure 3. Ca μ-XRF maps collected at SSRL beamline 2-3 (with scanning conditions optimized for Fe species) from cross sections of post-reaction Marcellus-PA. Higher signals are shown in warmer color. Signals at shale edges are lower because $CaCO_3$ is dissolved at these zones.

Contrary to Marcellus-PA, Eagle Ford contains substantial carbonate. SEM-BSE images for post-reaction Eagle Ford under Condition 1 (**Figure 4**) show a dissolution front where porosity is enhanced due to carbonate dissolution. The BSE image of a cross section of the Eagle Ford core reacted under Condition 2 is shown in **Figure 5**. Barite fills microcracks and also forms (sub)micrometer veins in the matrix. For both Conditions, the dissolution fronts are about 30 – 50 μm into the shale matrix.

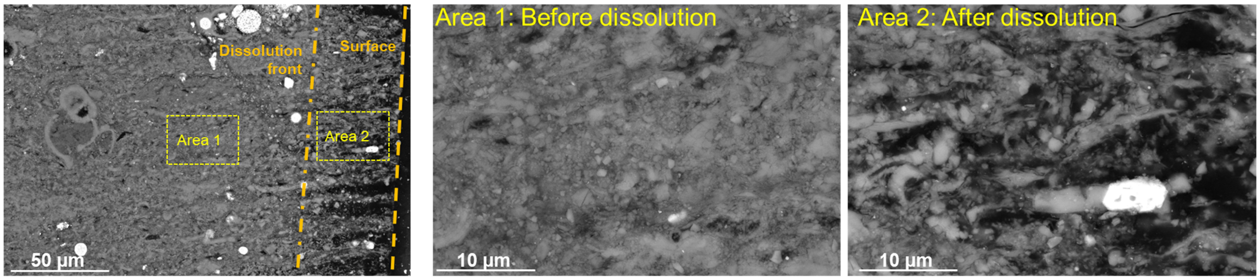

Figure 4. SEM-BSE images of a cross section from the Eagle Ford core reacted under Condition 1. Area 1 and Area 2 are zoomed in to show texture difference before and after carbonate dissolution, respectively.

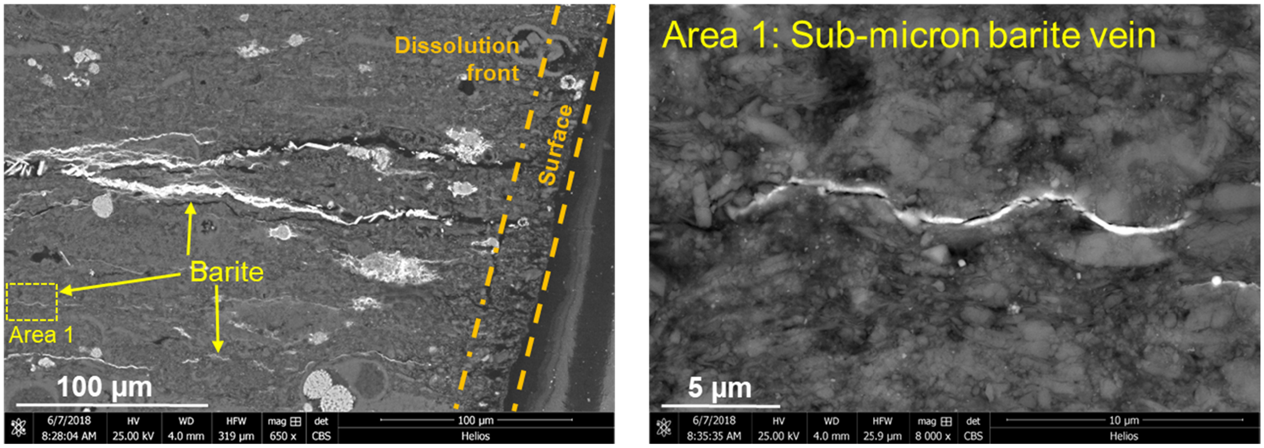

Figure 5. SEM-BSE images of a cross section from the Eagle Ford core reacted under Condition 2. Area 1 is zoomed in to show a representative sub-micrometer barite vein in shale matrix.

Plans for the next quarter:

- Draft journal manuscript on shale matrix reactions.

Task 3&4 (b): Measuring permeability alteration induced by fracture fluid reaction

For oil/gas production, alteration of the fracture surface microstructure modifies matrix permeability and thus production. In this section, we look at how large is the shale altered zone that is in contact with the reaction fluid and where is it predominantly occurring. We acquired µ-CT imaging of the post-reaction samples to show the altered zone and localization to determine where most of the reaction front is focused on. Once the imaging was complete, we performed an assortment of fluid penetration measurements to quantify the porosity changes occurring to the sample. These experiments give us insights showing direct relation of fracture fluid reaction impact on permeability and the SEM/EDS results we have shown in previous reports.

Table 3: Objectives in Tasks 3&4 (b) for Quarter 7.

Goal	Status
µ-CT imaging of post-reaction Marcellus core collected.	Complete
µ-CT imaging of post-reaction Eagle Ford core collected.	Complete
Porosity measurements for both Eagle Ford and Marcellus collected	Complete

Progress in Quarter 7:

Permeability measurements of two shale samples of varying carbonate concentrations were taken before and after reaction with acidic hydraulic fracturing fluid. Following permeability measurements and SEM imaging with Energy Dispersive Spectroscopy (EDS) analysis, we performed µ-CT imaging on both post-reaction samples to image the depth of penetration of the fracture fluid reaction front onto the shale matrix and measure the altered zone length over the reaction duration. This will provide us with insight on where the fluid is concentrated and pushed into the shale matrix. Afterwards we calculated pre- and post-reaction porosity changes on both samples using an assortment of fluid penetration measurements. Results are listed in **Table 4.**

Results in Quarter 7:

In previous reports we showed barite precipitation occurring in shale matrices and microcracks for both sample sets. Because this only showed precipitation, we wanted to investigate the total depth of barite precipitation into both the shale matrix and microcracks including understanding the dissolution-to-precipitation rates occurring for each sample set. To answer this question, we acquired 3D reconstructed x-ray CT imaging of the post-reaction shale samples and segment the reconstructed 3D core into 2 main regions: a shale matrix + microcracks region (green) and the fracture fluid reaction (yellow).

In **Figures 6 and 7**, we highlight a panel view comparison for each sample, where each column is showing a 2D XY plane view of the reacted core plug surface (left column), 3D reconstructed volume (middle column), and a 2D XZ plane view showing the depth of barite penetration into the shale matrix and microcracks (right column). The top row of the figure is image displayed in greyscale intensity, while the bottom row image is displayed in segmented color regions representing shale matrix versus reacted shale. All 3D volumes are reconstructed with 20µm x 20µm x 20µm voxel size.

For the Marcellus sample, as seen in **Figure 6**, we can see the post-reacted Marcellus core top view (left column) and microcore 3D volume (middle column) showing microcrack distribution of the shale sample and the bright regions signifying the altered zone being imaged. By segmenting the 3D volume into shale matrix and microcracks (green) as a single volume, we can isolate the reacted zone with the high concentration of alterations and reactions (yellow) generated across the microcore (right column). We measure the depth of penetration of barite precipitation along the reacted zone to be around 800µm, as shown from the 2D cross sectional view A-A' (bottom right).

We compare our findings to the reconstructed 3D CT volume of the Eagle Ford microcore, as shown in **Figure 7**. There is more overall alteration, coupled with thicker altered zone, in the Eagle Ford shale matrix and microcracks than in the Marcellus sample. This corresponds to higher dissolution-to-precipitation rates observed from PSD measurements and SEM/EDS imaging. Since most of the reacted shale surface is dissolved and altered, more precipitation will occur at to deeper depths into the shale matrix due to the presence of microcracks (bottom right).

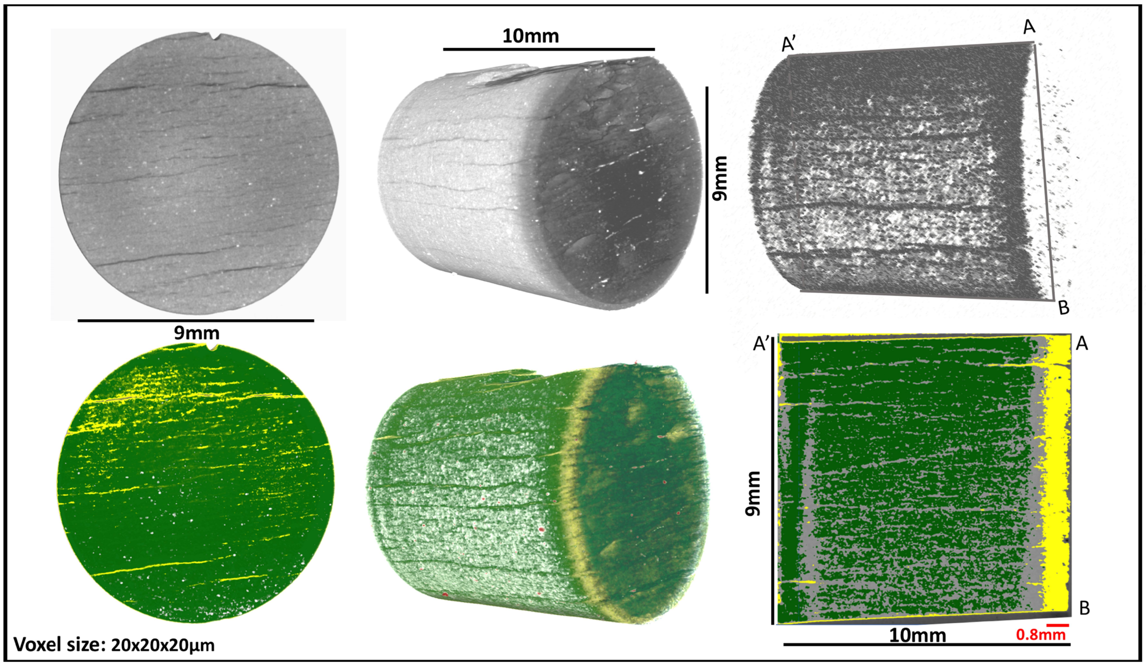

Figure 6: Reconstructed 3D volume from x-ray CT imaging for Marcellus microcore measured with voxel size: 20x20x20µm in greyscale intensity (top row) and color segmented volumes (bottom row). The segmented volumes are colored coded into two main regions: shale matrix and microcracks (green) and reacted zone (yellow). A 2D cross sectional planar view highlighting the depth of penetration of the fracture fluid and barite precipitates into the microcracks is measured around 800µm.

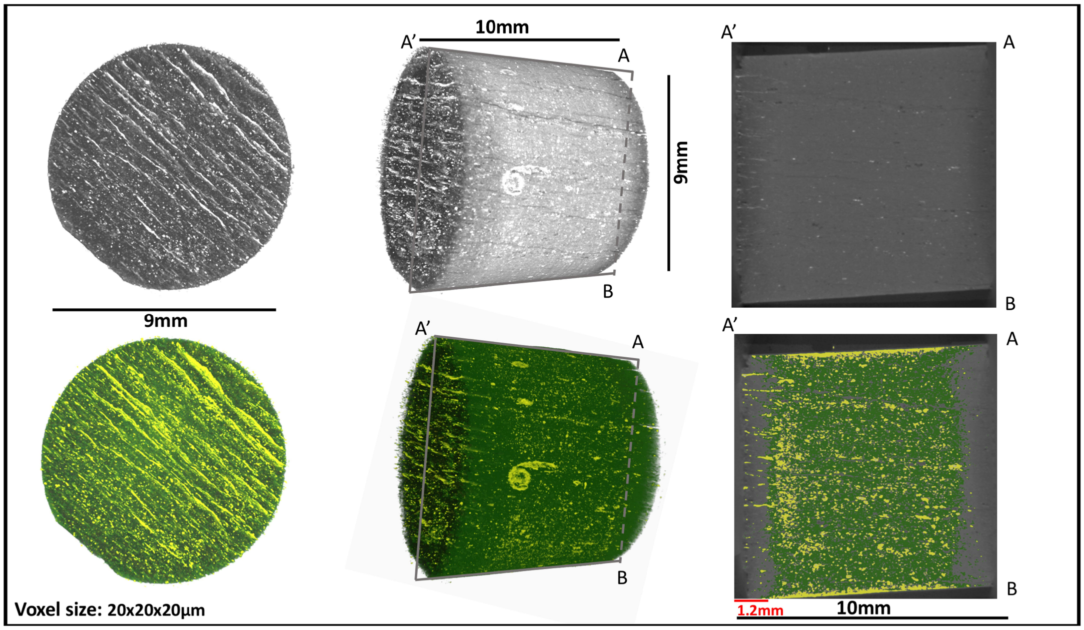

Figure 7: Reconstructed 3D volume from x-ray CT imaging for EagleFord microcore measured with voxel size: 20x20x20µm in greyscale intensity (top row) and color segmented volumes (bottom row). The segmented volumes are colored coded into two main regions: shale matrix and microcracks (green) and reacted zone (yellow). A 2D cross sectional planar view highlighting the depth of penetration of the fracture fluid and barite precipitates into the microcracks is measured around 1200µm.

We further examined the depth of altered zone into the microcracks for the Eagle Ford microcore by looking at a higher resolution interior tomographic image of a region with high fracture fluid and shale reaction concentration, as shown in **Figure 8**, (finer resolution of 1.8 x 1.8 x 1.8µm voxel size). This higher resolution 3D reconstructed volume shows that the depth of penetration into the microcracks to be around 1200µm. This high depth of penetration could be associated to the secondary porosity generation caused by dissolution of carbonate minerals along the surface area in contact with the fracture fluid during reaction, increasing along the microcracks (right). The slight difference in depth of penetration of the barite precipitates between the Eagle Ford and Marcellus shale samples could provide some insight on how the kinetics (rate) of dissolution-to-precipitation can be affected by shale matrix mineral composition and/or controlled by altering the fracture fluid chemical recipe.

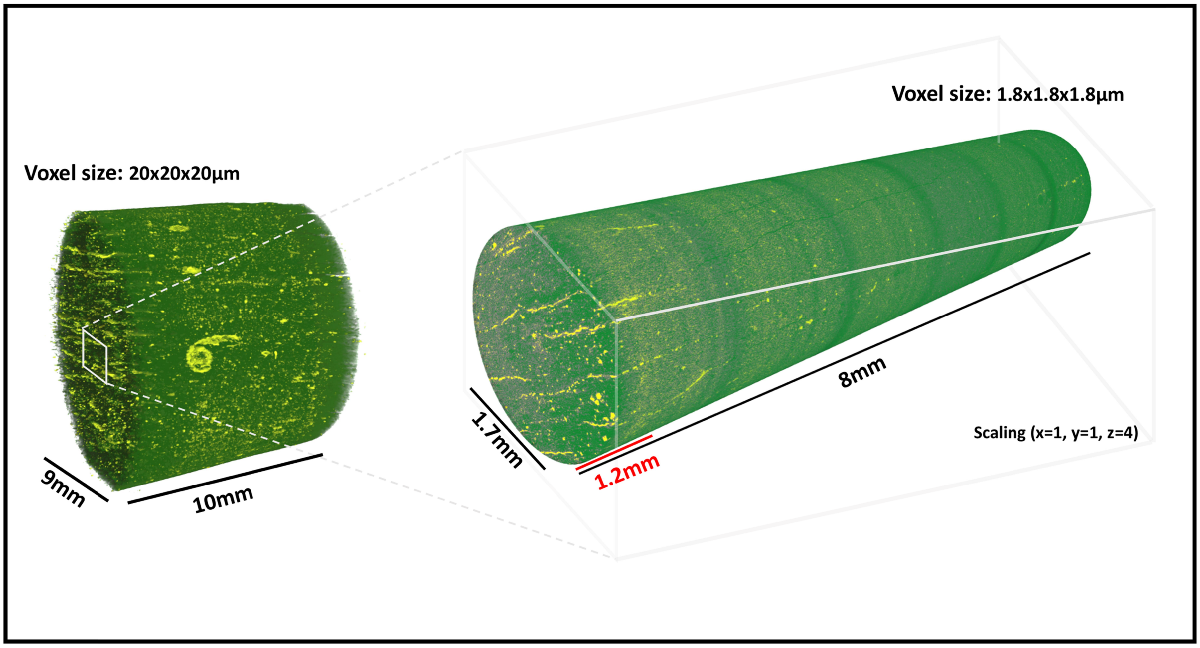

Figure 8: High resolution interior tomography of Eagle Ford from reconstructed 3D volume for a region of interest with high concentration of fracture fluid reactions on shale with voxel size: 1.8x1.8x1.8µm. The microcore sample length is vertically exaggerated 4x the diameter length. Color coded segmented volume highlighting the depth of penetration of the fracture fluid (yellow) into the shale matrix and microcracks (green) is measured around 1200µm.

In an attempt to quantify the pore alteration occurring in the shale matrix post-reaction, we conducted a series of fluid penetration measurements to measure the total accessible pore space available in the shale matrix. Results are listed in **Table 4**. We can infer from each measurement specific details about both the pore and mineral alterations occurring on each sample.

We notice an increase in the sample grain density for both Eagle Ford and Marcellus. This increase can be attributed to the precipitation of barite in both the shale matrix and into microcracks. Both sample sets show an increase in calculated porosity (%volume) and calculated pore volume (cc/g) from mercury porosimetry due to ongoing dissolution of the shale matrix from the fracture fluid reaction. The difference in the magnitude of sample porosity can be attributed to the mineral composition difference between both samples, which influences both dissolution rate and total system pH. Since the Eagle Ford sample is predominantly made up of carbonates, it had a higher dissolution-to-precipitation rate, which generated more secondary porosity porosity compared to the low-carbonate/high-clay Marcellus sample. Calculated bulk density gives us an idea of the dissolution-to-precipitation rates (kinetics) occurring in each sample throughout the reaction time with the fracture fluid. The Eagle Ford sample shows the bulk density to decrease post-reaction to fracture fluid, suggesting porosity opening reactions dominate, while bulk density increases for the Marcellus sample, suggesting porosity occluding reactions dominate. These observations help to explain – at the microstructural level – the observed permeability behavior (reported in Quarter 6). The increased porosity in Eagle Ford supports higher permeability, whereas loss of permeability in the Marcellus shale attenuates permeability.

Table 4. Measured pore size distributions from fluid penetration measurements for pre- and post-reaction shales.

	Eagle Ford		Marcellus		Measurement Tool (Method)
	Pre-reaction	Post-reaction	Pre-reaction	Post-reaction	
Grain Density (g/cc)	2.24	2.47	2.30	2.35	Helium Pycnometry (Gas Displacement Method)
Calculated Porosity via Density (%vol)	3.10	7.8	2.15	3.00	Mercury Porosimetry (Washburn Equation)
Calculated Pore Volume from MICP (cc/g)	0.013	0.034	0.009	0.013	
Bulk Density (g/cc)	2.34	2.28	2.25	2.28	

Planned Experiments in the next quarter:

- No further experiments are planned

Manuscript Plans for Tasks 3&4(b).

URTeC 2018 extended abstract "Effects of Hydraulic Fracturing Fluid Chemistry on Shale Matrix Permeability" has been published and presented.

Task 3&4 (c): Reactive transport modeling of shale-fluid interactions

Manipulation of reactions occurring *in-situ* in shale reservoirs will require a firm understanding of the rates of reactions. Iron dissolution and oxidation are two such important reactions, which help control iron scale precipitation. In our previous work, we showed qualitatively that organics naturally present in shale (bitumen) helped to accelerate iron oxidation by orders of magnitude, but we did not develop a rate law that can be used to quantify and ultimately predict this process in shales. In Quarter 7, we developed a kinetic rate law for bitumen-catalyzed Fe(II) oxidation. In this quarter we incorporated this rate law into a chemical model to simulate the shale sands experiments published in Harrison *et al.* (2017) [5] and in Jew *et al*, (2017) [6]. The modeling allows us to simulate the chemical reaction network in these experiments and refine reaction kinetics of the bitumen-catalyzed Fe(II) oxidation pathway.

Results in Quarter 7:

Barite precipitation

The mineralogical composition of New York Marcellus and Eagle Ford shales used in the shale "sand" experiments were previously reported in Harrison *et al.* (2017) [5] and Jew *et al*, (2017) [6]. Note: overall compositions differ between reported values for sand and whole-core experiments. In the shale "sand" experiments, 150 – 250 μm particles were prepared and 1 g submerged in 200 mL of synthetic fracture fluid, with a 50 mL headspace above the fracture fluid. The reaction lasted 3 weeks at 80^o C and 1 bar without agitation, and time-resolved samples were collected. More details about experimental materials and methods can be found in Harrison *et al.* (2017) [5] and Jew *et al*, (2017) [6].

Table 5. Objectives in Tasks 3&4 (c) for Quarter 7

Goal	Status
Build a chemical model to simulate Marcellus and Eagle Ford sand experiments performed in 2016 and 2017	Complete

Chemical modeling was carried out using the reactive transport modeling software package CrunchFlow [7]. A closed-system batch model consisting of a single grid cell characterized by the experimental fluid volume and rock mass was developed to reflect the experimental setup. The major aqueous species we focus on in the numerical simulation include pH, Ca^{2+} from carbonate dissolution, SO_4^{2-} from pyrite oxidation, and total aqueous Fe controlled by the balance between pyrite dissolution, Fe(II) oxidation, and Fe(III)-(hydr)oxide precipitation.

Mineral composition reported in volume percentages ($\frac{mineral}{shale} \times 100\%$) in **Table 6** is calculated from that reported in Harrison *et al.* (2017) [5] and Jew *et al* (2017) [6], assuming all minerals are similar in density. The mineral volume percentages used in model, also reported in **Table 6**, were originally based on the measured values. However, because the overall reaction rate is a product of the mineral volume, reactive surface area, and reaction affinity, in order to match the observed reaction rates required the adjustment of total mineral volumes, indicating some of the minerals in the shale were not accessible to the fluid. Several minerals commonly found in shale, but not detected using XRD, were also included (based on mass balance comparisons between the model and experiments). These mineral percentages are then multiplied by the volume fraction of shale sands in the reaction medium (e.g., 0.2 vol% shale sands in 200 mL fracture fluid) to yield the initial mineral fraction used in the single reaction cell in the model. The initial aqueous composition used in the model is the same for both Marcellus and Eagle Ford systems, as shown in **Table 7**. The fraction of bitumen was estimated with the assumption that bitumen content is about 10 ppm in shale with a density of 0.9 g/cm^3. The amount of bitumen does not affect the Fe(II)-oxidation rate because the rate law for bitumen-catalyzed Fe(II)-oxidation is not sensitive to the absolute amount of bitumen as long as bitumen is present.

Table 6. Mineral volume percentages measured in experiments compared to values required to reproduce observed mass balance using the model simulations. The decrease in model values relative to measured can be interpreted to reflect the fluid-accessible volume relative to the total or bulk volume.

	Marcellus		Eagle Ford	
Minerals	Measured (%)	Model (%)	Measured (%)	Model (%)
Pyrite	6.4	0.91	2.7	0.7
Calcite	11.6	9.5	64.5	70.0
Dolomite	1.1	1.1	-	-
Clay (illite)	35.0	35.0	7.6	7.6
Feldspar (albite)	3.7	0.56	-	-
Quartz	42.2	42.2	25.2	25.2
SiO_2(am)	-	0.20	-	0.20
Siderite	-	0.25	-	-
Hematite	-	0.0025	-	0.0025
Bitumen	-	0.0020	-	0.0020

Table 7. Initial aqueous composition for fracture fluid in the model

Species	Value	Notes
pH	2	Tuned with HCl in the experiment
Cl^-	408 ppm (1.15×10^{-2} M)	Calculated from charge balance
$O_{2(aq)}$ *	8 ppm (2.56×10^{-4} M)	Equilibrated with atmospheric O_2 at 25 °C
$CO_{2(aq)}$ **	0.6 ppm (1.40×10^{-5} M)	Equilibrated with atmospheric CO_2 at 25 °C
Organics	10 ppm	Combines all organic chemicals added to the fracture fluid
* Allow additional O_2 (in headspace or diffused from outside of the reactor) dissolving into solution during reaction. ** Allow CO_2 generated from $CaCO_3$ dissolution to partition between the fracture fluid and the reactor headspace during reaction, according to Henry's Law.		

Key reactions and parameters used in the model are listed in **Table 8**. Most aqueous chemical reactions involving the formation of aqueous complexes are described by equilibrium relationships, except the Fe(II)-oxidation reaction which is known to be a kinetically limited reaction. As reported in **Quarter 6 Report**, the Fe(II) oxidation occurs in two pathways, namely the H^+-dependent pathway and the bitumen-dependent pathway. Both the pathways are incorporated into the model to simulate shale-fluid interactions. The aqueous Fe(II) oxidation reaction rate is written as (variables are defined at top of page 17, where text continues):

$$\text{Rate} = k \cdot \prod (a)^{\nu} \cdot \left(\frac{Q}{K_{\text{eq}}} - 1\right) \qquad \text{Eq.1}$$

Table 8. Key reactions and parameters in the model at 80 °C

Speciation reactions

Species	Reaction	logK$_{eq}$
H	$H^+ + OH^- \leftrightarrow H_2O$	12.60
	$HCl_{(aq)} \leftrightarrow H^+ + Cl^-$	-0.64
	$CO_{2(aq)} + H_2O \leftrightarrow H^+ + HCO_3^-$	-6.30
	$CO_3^{2-} + H^+ \leftrightarrow HCO_3^-$	10.08
	$H_2S_{(aq)} \leftrightarrow H^+ + HS^-$	-6.54
	$H_2SO_{4(aq)} \leftrightarrow SO_4^{2-} + 2H^+$	1.02
Ca	$CaOH^+ + H^+ \leftrightarrow Ca^{2+} + H_2O$	12.85
	$CaCl^+ \leftrightarrow Ca^{2+} + Cl^-$	0.49
	$CaCl_{2(aq)} \leftrightarrow Ca^{2+} + 2Cl^-$	0.54
	$CaSO_{4(aq)} \leftrightarrow Ca^{2+} + SO_4^{2-}$	-2.38
Fe(II)	$FeOH^+ + H^+ \leftrightarrow Fe^{2+} + H_2O$	7.87
	$Fe(OH)_{2(aq)} + 2H^+ \leftrightarrow Fe^{2+} + 2H_2O$	17.23
	$FeCl^+ \leftrightarrow Fe^{2+} + Cl^-$	-0.070
	$FeCl_{2(aq)} \leftrightarrow Fe^{2+} + 2Cl^-$	2.02
	$FeCO_{3(aq)} + H^+ \leftrightarrow Fe^{2+} + HCO_3^-$	5.60
	$FeHCO_3^+ \leftrightarrow Fe^{2+} + HCO_3^-$	-2.72
	$FeSO_{4(aq)} \leftrightarrow Fe^{2+} + SO_4^{2-}$	-2.20
Fe(III)	$FeOH^{2+} + H^+ \leftrightarrow Fe^{3+} + H_2O$	1.34
	$Fe(OH)_2^+ + H^+ \leftrightarrow Fe^{3+} + 2H_2O$	4.73
	$Fe(OH)_{3(aq)} + 3H^+ \leftrightarrow Fe^{3+} + 3H_2O$	12.95
	$FeCl^{2+} \leftrightarrow Fe^{3+} + Cl^-$	-0.36
	$FeCl_2^+ \leftrightarrow Fe^{3+} + 2Cl^-$	-2.13
	$FeCO_3^+ + H^+ \leftrightarrow Fe^{3+} + HCO_3^-$	1.73
	$FeSO_4^+ \leftrightarrow Fe^{3+} + SO_4^{2-}$	-3.00
Al	$AlOH^{2+} + H^+ \leftrightarrow Al^{3+} + H_2O$	3.52
	$Al(OH)_2^+ + 2H^+ \leftrightarrow Al^{3+} + 2H_2O$	7.82
	$AlSO_4^+ \leftrightarrow Al^{3+} + SO_3^{2-}$	-3.01
Mg	$MgCl^+ \leftrightarrow Mg^{2+} + Cl^-$	-0.048
	$MgCO_{3(aq)} + H^+ \leftrightarrow HCO_3^- + Mg^{2+}$	6.73

Fe(II) oxidation aqueous kinetic reactions

Pathway	Reaction	$\prod(a)^{\nu}$	logK$_{eq}$	logk
H^+-dependent	$Fe^{2+} + H^+ + 0.25O_{2(aq)} \rightarrow Fe^{3+} + 0.5H_2O$	$(Fe^{2+})^{1.0}(O_{2(aq)})^{1.0}(H^+)^{-2.0}$	0.938	-5.82
Bitument-dependent		$(Fe^{2+})^{1.0}(O_{2(aq)})^{1.0}(Bitumen)^{0.1}$		5.9 for Marcellus; 7.9 for Eagle Ford

Mineral kinetic reactions

Mineral	Reaction	$\prod(a)^{\nu}$	logK$_{sp}$	logk
Pyrite	$Pyrite + H_2O + 3.5O_{2(aq)} \rightarrow 2H^+ + 2SO_4^{2-} + Fe^{2+}$	$(O_{2(aq)})^{0.5}(H^+)^{-0.11}$	217	-8.0 for Marcellus; -8.5 for Eagle Ford
Calcite	$Calcite + H^+ \rightarrow Ca^{2+} + HCO_3^-$	$(H^+)^{1.0}$	1.05	-5.5
Dolomite	$Dolomite + 2H^+ \rightarrow Ca^{2+} + Mg^{2+} + 2HCO_3^-$	$(H^+)^{0.5}$	0.70	-7.5
Clay (illite)	$Illite + 8H^+ \rightarrow 0.25Mg^{2+} + 0.6K^+ + 2.3Al^{3+} + 3.5SiO_{2(aq)} + 5.0H_2O$	None	3.79	-11.0
Feldspar (albite)	$Albite + 4H^+ \rightarrow Al^{3+} + Na^+ + 2H_2O + 3SiO_{2(aq)}$	None	0.93	-11.0
Quartz	$Quartz \rightarrow SiO_{2(aq)}$	None	-3.24	-15.0
$SiO_{2(am)}$	$SiO_{2(am)} \rightarrow SiO_{2(aq)}$	None	-2.27	-7.2
Siderite	$Siderite + H^+ \rightarrow Fe^{2+} + HCO_3^-$	None	-1.17	-7.0
Hematite	$Hematite + 6H^+ \rightarrow 2Fe^{3+} + 3H_2O$	None	-4.94	-8.0
Bitumen	$Bitumen_{(s)} \rightarrow Bitument_{(aq)}$	$(Organics)^{1.0}$	-1.30	-2.3

where k is the reaction constant in mol/kg of water/yr, $\prod(a)^{\nu}$ is the product of all aqueous species that the rate is dependent on, where a is the activity of the aqueous species, and ν is the empirical exponent indicating the extent of dependency. Q is the ion activity product, and K_{eq} is the equilibrium constant for the Fe(II) oxidation reaction. The rate formula for Fe(II) oxidation in the aqueous phase is based on that obtained in Quarter 6, with the rate constant k tuned for Marcellus and Eagle Ford to fit the experimental data.

The mineral reactions are all mixed equilibrium-kinetic reactions. The rate laws for mineral reactions are based on Transition State Theory (TST) style of rate law, written as

$$\text{Rate} = A \cdot k \cdot \prod(a)^{\nu} \cdot \left(\frac{Q}{K_{\text{sp}}} - 1\right) \qquad \text{Eq. 2.}$$

In Eq. 2, A is the specific surface area (m^2/g), k is the rate constant (mol/m^2 of mineral surface area/s), $\prod(a)^{\nu}$ is the rate dependency similar to that defined for the Eq. 1 and K_{sp} is the equilibrium constant for the mineral. Because A and k are multiplied, we assume A is constant and report all the rate variation in the rate constant k. A positive rate indicates precipitation of the mineral, and a negative rate indicates dissolution.

We choose the time-resolved values for pH, and concentrations of Ca, Fe, and S to fit the experimental data, because these are the most critical species for dissolution and precipitation. **Figure 9** shows the modeling results compared to experimental results for Marcellus and Eagle Ford.

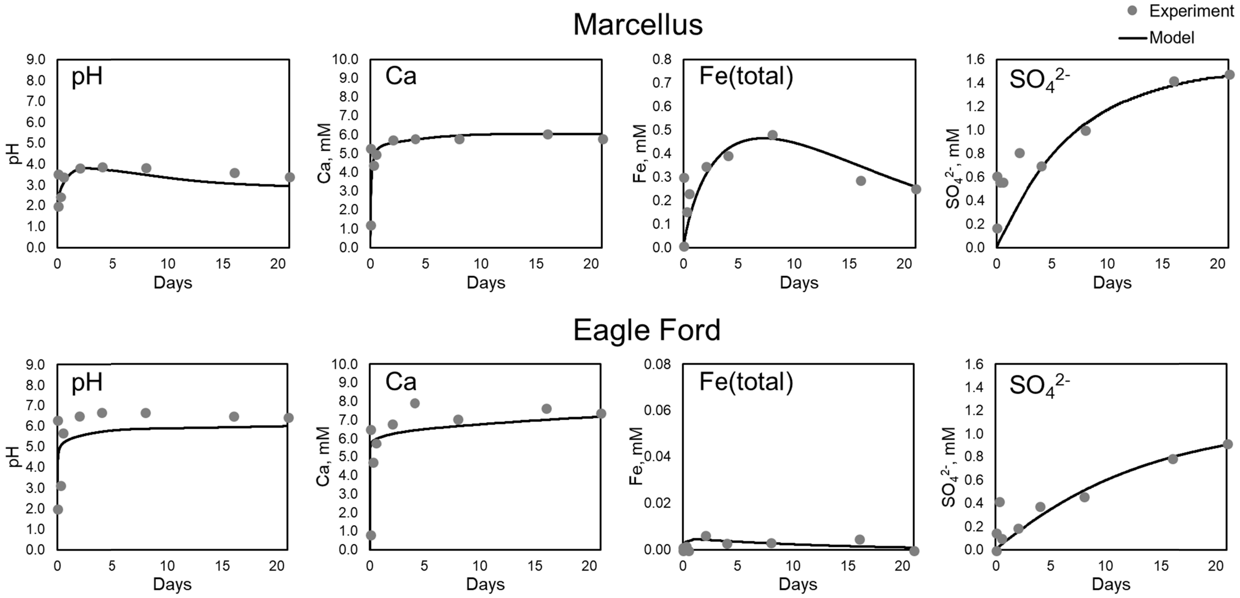

Figure 9. Modeling results (lines) compared to experimental data (dots) for Marcellus (top row) and Eagle Ford (bottom row).

The pH of the Marcellus system increased rapidly during the early reaction period due to carbonate dissolution, consistent with a rapid increase in Ca concentration from carbonate dissolution. The Ca concentration plateaus within several days once all carbonate is depleted. The pH of the system after about 5 days then drops gradually due to two competing reactions: the

Fe(III) (hydr)oxide precipitation that produces H^+ and decreases pH (as demonstrated in Quarter 6 Report Task 3&4 (c)), and the dissolution of clay and feldspar that consumes H^+.

As shown in the Fe figure for Marcellus, the Fe concentration increases at the beginning of the reaction due to mineral dissolution. Most of the Fe is dissolved from pyrite but including a small amount (lower than XRD detectable content) of siderite in the model is required to capture the rapid initial increase in the Fe concentration. The Fe concentration drops after a couple of days due to Fe(II)-oxidation and Fe(III) (hydr)oxide precipitation.

Unlike the Marcellus system, the modeling results for pH evolution in the Eagle Ford system are lower by about 1 pH unit relative to the pH measured in the Eagle Ford experiments. Even though the model predicts that 81.5% of carbonate is still present at the end of the reaction, the model does not predict further carbonate dissolution to increase pH. To explain this pH discrepancy, one needs to consider the difference between *in situ* condition (*i.e.*, what the model predicts) and the measurement condition (*i.e.*, the condition when the aqueous solution was analyzed in the experiments). During the reaction, the reactor was sealed with a rubber cap, allowing limited gas diffusion (if any) across the reactor boundaries. As the carbonate was dissolving, CO_3^{2-} released from the solid phase increased the CO_2 fugacity. The CO_2 would escape from the solution and accumulate in the reactor headspace according to Henry's law. A mass balance calculation showed that with 200 mL reaction fluid and 50 mL headspace, the end pH for the Eagle Ford reaction solution before CO_2 degasses should be pH 6.1 (lower than experimentally measured pH), as shown by the solid line in **Figure 9**. In the experiments, the pH measurements were conducted after a liquid sample was transferred out of the reactor. During the sampling process, more CO_2 degassed from the solution, and pH should increase somewhat to higher values. Thus, we conclude that the model-data discrepancy in pH (about 0.5 pH units) is due to CO_2 degassing prior to measurement.

To match the experimentally measured Fe concentration in the Eagle Ford system also required an increase in the rate constant (k) for the bitumen-catalyzed Fe(II)-oxidation. The high pH and the time lapse between sampling and measurement for the Eagle Ford system could be a possible explanation for the higher rate constant (8×10^7 mol/kg of water/yr, compared to 8×10^5 mol/kg of water/yr for the Marcellus system). However, it is also possible that the *in situ* Fe concentrations were higher than the concentrations measured after sampling, because after sampling the solution could have further reacted with O_2 and experienced pH increase due to CO_2 degassing, both processes favoring Fe(II) oxidation and precipitation that lowers the aqueous Fe concentration. Another explanation for the different rates of bitumen-catalyzed oxidation between the Marcellus and Eagle Ford systems is the bitumen itself. As bitumen is a composite of organic-soluble organic compounds in shale without a standard chemical formula, the composition can vary considerably from shale to shale. The bitumen used to study Fe(II) oxidation in shale-free systems (*i.e.*, the experiments simulated in Quarter 6) was extracted from Marcellus, and a k value of 8×10^5 mol/kg of water/yr was obtained from modeling. It is possible that the bitumen in Eagle Ford has greater catalytic potential for Fe(II)-oxidation.

From modeling of both Marcellus and Eagle Ford "sand" experiments, three new insights emerge regarding pyrite oxidation and Fe(III)-scale formation:

First, the fracture fluid has limited access to the majority of pyrite. The sulfate concentrations measured from both the Marcellus and Eagle Ford experiments show a rapid increase at the beginning of the reaction followed by a decrease in net release at later times, suggesting that pyrite dissolution at a later time point was limited by diffusion. This is reasonable because the shale sands used in the experiment were 150 – 250 μm in diameter, and the pyrite grains imbedded inside the sand particles may have been protected by the low matrix diffusivity – especially for the outcrop shale with no microcracks. To capture the limited accessibility of pyrite by fracture fluid, the fractions of pyrite in shale had to be decreased by 86% for Marcellus (i.e., 14% of the total pyrite was dissolved) and 74% for Eagle Ford (i.e., 26% of the total pyrite was dissolved).

Second, dissolved O_2 is the limiting factor for Fe(II)-oxidation, and continuous supply of O_2 from the air in the reactor headspace (including O_2 slowly diffusing from the reactor cap) is critical in obtaining the Fe(II) oxidation kinetics observed in the experiments. Without this supply of O_2 into the fracture fluid, the initial dissolved O_2 in the fracture fluid is not sufficient to dissolve the amount of pyrite observed in the experiment, nor is it sufficient to allow for Fe(III) to be removed as Fe(III) (hydr)oxides (**Figure 10**). In field-scale hydraulic fracturing systems, continuous injection of fracturing fluid is the source of dissolved O_2 to oxidize Fe(II).

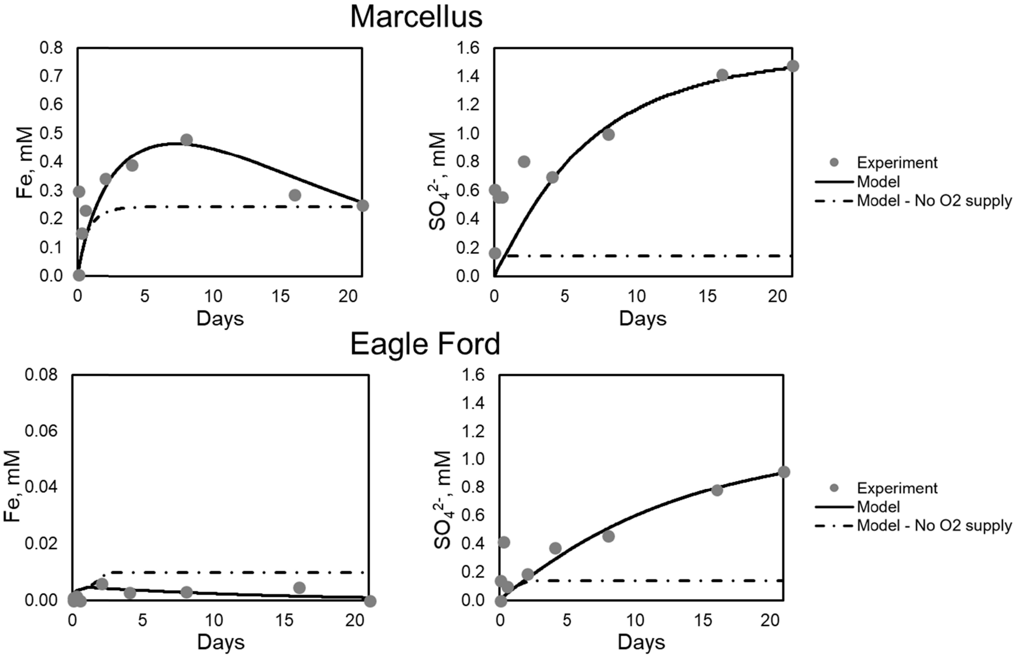

Figure 10. Without continuous supply of O_2, the initial amount of dissolved O_2 in the fracture fluid in the experiments is not sufficient to dissolve pyrite and oxidize Fe(II). Note the order-of-magnitude difference in Fe concentrations between Marcellus and Eagle Ford.

Even with the continuous supply of O_2 into the fracture fluid, the concentration of dissolved O_2 remains low due to consumption of O_2 by pyrite dissolution, resulting in limited oxidation of Fe(II) to Fe(III). Therefore, almost all aqueous Fe stays in the Fe(II) form. The ratio of Fe(II) to Fe(III) in the aqueous solution is shown in **Figure 11**. As a result, the saturation index ($\log_{10}(Q/K_{sp})$) for hematite remains close to 0 (i.e., near equilibrium) for both systems.

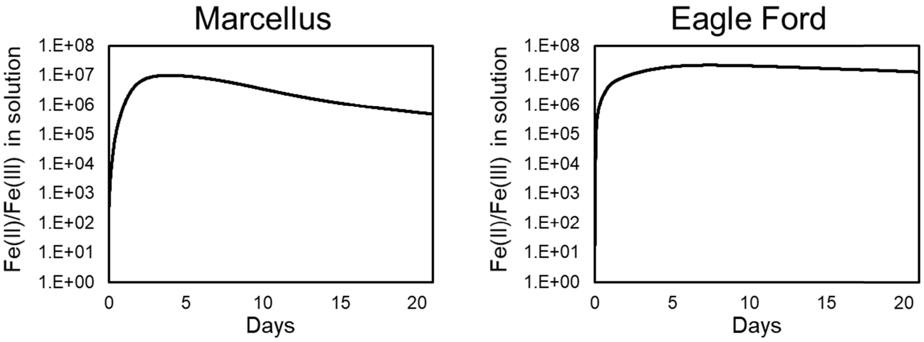

Figure 11. Ratio of Fe(II) to Fe(III) in the aqueous phase. Almost all Fe stays in the Fe(II) form.

Third, as expected, the bitumen-catalyzed Fe(II) oxidation is important for the Fe dynamics in the fracture fluid. The importance of this bitumen-dependent pathway is quantified by comparing the simulation results with and without including this pathway. As shown in **Figure 12**, if we do not consider the bitumen-catalyzed Fe(II)-oxidation mechanism, Fe(II)-oxidation is slower in the Eagle Ford system, and hardly occurs in the low pH Marcellus system.

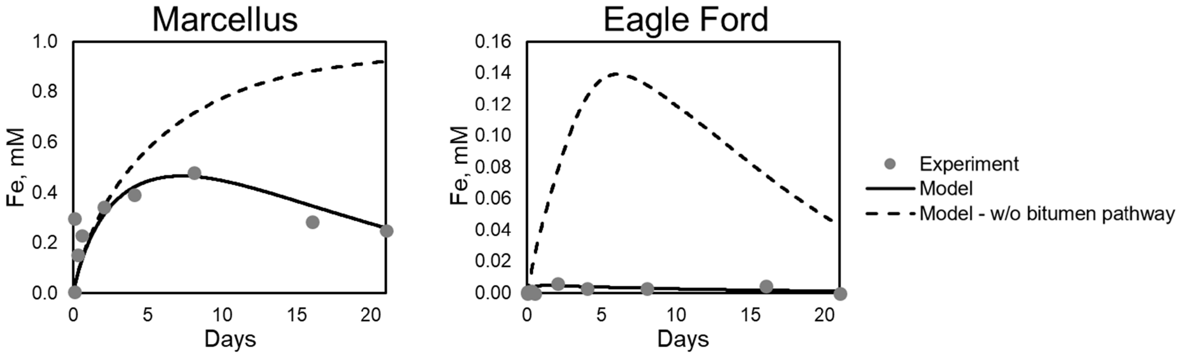

Figure 12. The bitumen-catalyzed Fe(II) oxidation pathway is important for both Marcellus and Eagle Ford systems. Note the difference in Fe concentrations between Marcellus and Eagle Ford.

Plans in the next quarter:

- Complete the development of the reactive transport model for shale matrix reactions using reaction networks developed above.

7. MISCELLANEOUS

A new project FWP was submitted to DOE-HQ. An initial manuscript draft for the U portion of the project from the initial 2-year project has been completed and sent to co-authors for edits. This manuscript is entitled: The Effect of Hydraulic Fracturing Fluid on the Stability of Uranium in Unconventional Oil/Gas Shales. This article is targeted for publication in the journal Environmental Science & Technology.

8. REFERENCES.

[1] Ghode, Roopali; Muley, Rajashree; Sarin, Rajkamal. *Operationally determined chemical speciation of barium and chromium in drilling fluid wastes by sequential extraction*. Chemical Speciation & Bioavailability, 7 (4) **1995**, 133-137.

[2] Neff, Jerry M. *US EPA Report: Fate and biological effects of oil well drilling fluids in the marine environment: A literature review*. **1981**, 1-178.

[3] Neff, Jerry M. *Estimation of bioavailability of metals from drilling mud barite*. Integrated Environmental Assessment and Management. 4 (2) **2008**, 184-193.

[4] Renock, Devon; Landis, Joshua D.; Sharma, Mukul. *Reductive weathering of black shale and release of barium during hydraulic fracturing*. Applied Geochemistry, 65, **2016**, 73-86.

[5] Harrison, A. L., Jew, A. D., Dustin, M. K., Thomas, D. L., Joe-Wong, C. M., Bargar, J. R., Natalie Johnson, Gordon E. Brown, Jr. Maher, K. *Element release and reaction-induced porosity alteration during shale-hydraulic fracturing fluid interactions*. Applied Geochemistry, 82, **2017**, 47-62.

[6] Jew, A. D.; Dustin, M. K.; Harrison, A. L.; Joe-Wong, C.; Thomas, D. L.; Maher, K.; Gordon E. Brown, J.; Bargar, J. R., *Importance of pH, Oxygen, and Bitumen on the Oxidation and Precipitation of Iron during Hydraulic Fracturing of Oil/Gas Shales*. Energy & Fuels 31(4), **2017**, 3643–3658. **DOI:** 10.1021/acs.energyfuels.6b03220

[7] Steefel, C. I. "CrunchFlow. Software for Modeling Multicomponent Reactive Flow and Transport. User's Manual."

9. RISK ANALYSIS

Task 1: No significant risks to report at this stage of the project.

Task 2: No significant risks to report at this stage of the project.

Task 3&4. No significant risks to report at this stage of the project.

10. MILESTONE STATUS

Activity and milestones	Verification method†	Planned Milestone Date	Actual completion or status
Task 1. Project management			
1.1 Development of PMP	D	10-31-16	10-28-16
1.2 Recruit postdoc / RA	D	4-30-17	10-30-17
1.3 Quarterly research performance reports	D	1-30-17‡	7-30-17
1.4 Annual research performance report	D	11-30-17*	11-30-17
1.5 Final technical report	D	11-30-18	
Task 2. Influence of dissolved organic compounds on precipitate formation/stability			
2.1 Research/evaluation of literature and detailed experimental design	D	1-30-17	12-23-16
2.2 Set-up and test stirred tank reactors	D	1-30-17	12-19-16
2.3 Complete initial scoping experiments to determine types of organic compounds for detailed measurement	D	4-30-17	3-13-17
2.4 Complete measurements of initial rates of solid precipitation	D	7-30-17	6-30-17
2.5 Identification of precipitate mineralogy	XRD, XAS, SEM	10-30-17	9-30-17
2.6 Complete measurement of shale sand dissolution	D	7-30-17	6-30-17
2.7 Complete solubility measurements	D	7-30-17	10-30-17
2.8 Dissolution rate measurements in presence of shale sands with coupled dissolution and precipitation	D	10-30-17	10-30-17
2.9 Complete initial draft of manuscript	D	4-30-18	4-30-18
2.10 Submit manuscript	D	7-30-18	7-30-18
Task 3. Impact of secondary pore networks on gas transport across shale matrix-fracture interfaces			
3.1 Research/evaluation of literature and design experiments favorable for secondary porosity generation	D	1-30-17	12-21-16
3.2 Submit beam time proposals	D	1-30-17	12-1-16
3.3 Acquire shale samples	D	1-30-17	11-9-16
3.4 Conduct telecons quarterly (as needed) with NETL group	N	1-30-17‡	Ongoing
3.5 Conduct telecons quarterly (as needed) with LANL group	**N**	1-30-17‡	Ongoing
3.6 Mineralogical characterization of shale samples	XRD, SEM	7-30-17	6-30-17
3.7 Measure gas permeability of unreacted cores	P	7-30-17	7-30-17
3.8 Collect μ-CT images for unreacted shale cores	μ-CT	7-30-17	3-7-17
3.9 Complete image processing for unreacted shale cores	D	10-30-17	10-30-17
3.10 Set up and test whole-core reactors: initial scoping experiments	D	7-30-17	11-30-16
3.11 Perform shale whole-core reactions	D	1-30-18	12-19-16
3.12 Collect μ-CT images on reacted cores	μ-CT	4-30-18	12-30-17
3.13 Collect XRM maps on thin section of unreacted and reaction cores	XRM, SEM	4-30-18	4-30-18
3.14 Measure gas permeability through reacted cores	P	4-30-18	4-30-18
3.15 Complete image processing and data analysis for reacted cores	D	9-30-18	In progress
3.16 Develop a shale sand batch reaction model to refine rate constants for new Fe(II) oxidation rate law	D	9-30-18	7-30-18
3.17 Complete initial draft of manuscript	D	9-30-18	
3.18 Submit manuscript	D	12-30-18	

Activity and milestones	**Verification method**[†]	**Planned Milestone Date**	**Actual completion or status**
Task 4. Impact of secondary precipitation on gas transport across shale matrix-fracture interfaces			
4.1 Research/evaluation of literature and design experiments favorable for secondary precipitation	D	1-30-17	12-21-16
4.2 Measure gas permeability of unreacted cores	P	7-30-17	7-30-17
4.3 Collect μ-CT images on unreacted shale cores	μ-CT	7-30-17	3-7-17
4.4 Complete image processing and analysis on unreacted shale cores	D	10-30-17	10-30-17
4.5 Set up and test whole-core reactors: initial scoping experiments	D	10-30-17	3-20-17
4.6 Perform shale whole-core reactions	D	4-30-18	4-30-18
4.7 Measure permeability of reacted cores	D	9-30-18	3-30-18
4.8 Collect μ-CT images on reacted cores	P, μ-CT	10-30-18	3-30-18
4.9 Collect XRM maps on thin section of unreacted and reaction cores	XRM, SEM	10-30-18	7-30-18
4.10 Complete image processing and data analysis for reacted cores	D	3-30-19	In progress
4.11 Develop a batch reaction model to refine rate constants for barite scale precipitation reactions	NM	10-30-18	3-30-18
4.12 Build a 1D reactive transport model for shale matrix-fluid interface reactions	D	12-30-18	In progress

[‡] Quarterly reports will follow every 3 months following starting date. * Annual reports are due every 12 months on Nov 30.

[†] Verification Method Key:

AF = Software for data processing and visualization (Avizo Fire)
D = Documentation or data
EELS = Electron energy loss spectroscopy
FIB-SEM = Focused ion beam – scanning electron microscopy
μ-CT = Micrometer-scale X-ray computed tomography
nano-CT= Nanometer-scale X-ray computed tomography
N = Note from meeting
NM = Numerical modeling
OP = Optical petrography
P = Pulse-decay permeability
SAXS = Small angle X-ray scattering
SANS = Small angle neutron scattering
SEM = Scanning electron microscopy
TEM = Transmission electron microscopy
TXMWiz = Software for data processing of transmission X-ray images (TXM Wizard)
XAS = X-ray absorption spectroscopy
XRM = X-ray microprobe
XRD = X-ray diffraction

11. SCHEDULE STATUS

All milestones for this quarter have been met. As of the time of writing, the project is on-schedule.

Changes to schedule and milestones in the past quarter: Qingyun Li (postdoc) is taking 2-month maternity leave from mid-June to mid-August. Since Qingyun is performing tasks 3&4(a) and (c), we have rescheduled the affected subtasks. These changes were anticipated and approved in May 2018 and noted in the report for Quarter 6 (May 15, 2018).

Cumulative modification explanation log for milestones list:

Report Date	Task	Planned date	Revised date	New Task goal / Explanation
5-15-18	3.15	7-30-18	9-30-18	Accommodate 2-month maternity leave
5-15-18	3.16	7-30-18	9-30-18	Accommodate 2-month maternity leave New task name: “Develop a shale sand batch reaction model to refine rate constants for new Fe(II) oxidation rate law”
5-15-18	3.17	7-30-18	9-30-18	Accommodate 2-month maternity leave
5-15-18	3.18	10-31-18	12-30-18	Accommodate 2-month maternity leave
5-15-18	4.10	1-31-19	3-30-19	Accommodate 2-month maternity leave
5-15-18	4.11	10-31-18	NA	New task name: Develop a batch reaction model to refine rate constants for barite scale precipitation reactions
5-15-18	4.12	NA	12-30-18	New task: Build a 1D reactive model for shale matrix-fluid interface reactions

Project timeline from the Project Management Plan. "M" denotes milestones.

Task	Title	Month of project																													
		2016			2017												2018												2019		
		1	2	3	4	5	6	7	8	9	10	11	12	13	14	15	16	17	18	19	20	21	22	23	24	25	26	27	28	29	30
		Oct	Nov	Dec	Jan	Feb	Mar	Apr	May	Jun	Jul	Aug	Sep	Oct	Nov	Dec	Jan	Feb	Mar	Apr	May	Jun	Jul	Aug	Sep	Oct	Nov	Dec	Jan	Feb	Mar
1	Project management plan																														
1.1	Development of PMP	■	■	■	■	■	■	■	■	■	■	■	■	■	■	■	■	■	■	■	■	■	■	■	■						
1.2	Recruit postdoc/RA	■	■	■	■	■	■	■																							
1.3	Quarterly research performance reports				■			■			■						■			■			■								
1.4	Annual research performance report														■												■				
1.5	Final technical report																										■				
2	Influence of dissolved organic compounds on precipitate formation/stability																														
2.1	Evaluate literature/ experimental design	■	■	■	■																										
2.2	Set-up and test stirred tank reactors	■	■	■	■																										
2.3	Complete initial scoping experiments				■	■	■	■																							
2.4	Complete measurements of initial rates of solid precipitation							■	■	■	■																				
2.5	Identification of precipitate mineralogy										■	■	■	■																	
2.6	Measure shale sand dissolution							■	■	■	■																				
2.7	Complete solubility measurements									■	■																				
2.8	Dissolution rate measurements in presence of shale sands										■	■	■	■																	
2.9	Complete initial draft of manuscript													■	■	■	■	■	■	■											
2.10	Submit manuscript																			■	■	■	■								
3	Impact of secondary pore networks on gas transport across shale matrix-fracture interfaces																														
3.1	Evaluate literature/ experimental design	■	■	■	■																										
3.2	Submit beam time proposals	■	■	■	■																										
3.3	Acquire shale samples	■	■	■	■																										
3.4	Quarterly (as needed) with NETL group				■			■			■						■			■			■								
3.5	Quarterly (as needed) with LANL group				■			■			■						■			■			■								
3.6	Mineral characterization shale samples				■	■	■	■	■	■	■																				
3.7	Measure permeability of unreacted cores				■	■	■	■	■	■	■																				
3.8	Collect μ-CT images, unreacted cores				■	■	■	■	■	■	■																				
3.9	Image processing, unreacted shale cores							■	■	■	■	■	■	■																	
3.10	Test whole-core reactors: Initial scoping experiments				■	■	■	■	■	■	■																				
3.11	Perform shale whole-core reactions										■	■	■	■	■	■	■														
3.12	Collect μ-CT images on reacted cores															■	■	■	■	■											
3.13	XRM maps, unreacted/ reacted cores				■	■	■	■	■	■	■	■	■	■	■	■	■	■	■	■											
3.14	Measure permeability of reacted cores															■	■	■	■	■											
3.15	Image processing, reacted shale cores																	■	■	■	■	■	■	■	■						
3.16	Develop a batch reaction model to refine rate constants for Fe(II) oxidation			■	■	■	■	■	■	■	■	■	■	■	■	■	■	■	■	■	■	■	■	■	■						
3.17	Complete initial draft of manuscript																	■	■	■	■	■	■	■	■						
3.18	Submit manuscript																					■	■	■	■	■	■	■			
4	Impact of matrix precipitation on gas transport across shale matrix-fracture interfaces																														
4.1	Evaluate literature/ experimental design	■	■	■	■																										
4.2	Measure permeability of unreacted cores				■	■	■	■	■	■	■																				
4.3	Collect μ-CT images, unreacted cores				■	■	■	■	■	■	■																				
4.4	Image processing, unreacted shale cores							■	■	■	■	■	■	■																	
4.5	Test whole-core reactors: Initial scoping experiments							■	■	■	■	■	■	■																	
4.6	Perform shale whole-core reactions												■	■	■	■	■	■	■	■											
4.7	Measure permeability of reacted cores																		■	■	■	■	■	■	■						
4.8	Collect μ-CT images on reacted cores																					■	■	■	■	■	■	■			
4.9	XRM maps, unreacted/ reacted cores																					■	■	■	■	■	■	■			
4.10	Image processing, reacted shale cores																							■	■	■	■	■	■	■	■
4.11	Develop a batch reaction model to refine rate constants for barite scale							■	■	■	■	■	■	■	■	■	■	■	■	■	■	■	■	■	■	■	■	■			
4.12	Build a 1D reactive model for shale matrix-fluid interface reactions							■	■	■	■	■	■	■	■	■	■	■	■	■	■	■	■	■	■	■	■	■			

12. COST STATUS

Cost Plan/Status

Basesline Reporting Quarter		Year 4	Start: 10/1/16 End: 9/30/17			Year 5	Start: 10/1/17 End: 9/30/18		
		Q1	Q2	Q3	Q4	Q5	Q6	Q7	Q8
Baseline Cost Plan									
Federal Share	Task 1	$ 9,686	$ 9,686	$ 9,686	$ 9,686	$ 12,750	$ 12,750	$ 12,750	$ 12,750
	Task 2	$ 31,681	$ 31,681	$ 31,681	$ 31,681	$ 44,625	$ 44,625	$ 44,625	$ 44,625
	Task 3	$ 42,400	$ 42,400	$ 42,400	$ 42,400	$ 35,700	$ 35,700	$ 35,700	$ 35,700
	Task 4	$ 23,733	$ 23,733	$ 23,733	$ 23,733	$ 34,425	$ 34,425	$ 34,425	$ 34,425
	Task 5								
	Task 6								
Non-Federal Share									
Total Planned Costs (Federal and Non-Federal)									
Cumulative Baseline Cost		$ 107,500	$ 215,000	$ 322,500	$ 430,000	$ 557,500	$ 685,000	$ 812,500	$ 940,000
Actual Incurred Costs									
Federal Share	Task 1	$ 7,290	$ 13,437	$ 8,509	$ 16,530	$ 14,370	$ 9,979	$ 12,291	
	Task 2	$ 25,514	$ 47,028	$ 29,782	$ 57,855	$ 50,294	$ 34,927	$ 43,019	
	Task 3	$ 20,411	$ 37,622	$ 23,826	$ 46,284	$ 40,236	$ 27,942	$ 34,415	
	Task 4	$ 19,682	$ 36,279	$ 22,975	$ 44,631	$ 38,799	$ 26,944	$ 33,186	
	Task 5	$ -	$ -	$ -	$ -	$ -	$ -	$ -	$ -
	Task 6	$ -	$ -	$ -	$ -	$ -	$ -	$ -	$ -
Non-Federal Share									
Total Incurred Costs - Quarterly (Federal and Non-Federal)									
Cumulative Incurred Cost		$ 72,898	$ 134,366	$ 85,093	$ 165,300	$ 143,698	$ 99,792	$ 122,912	$ -
Variance									
Federal Share	Task 1	$ 2,396	$ (3,750)	$ 1,177	$ (6,843)	$ (1,620)	$ 2,771	$ 459	$ 12,750
	Task 2	$ 6,167	$ (15,347)	$ 1,899	$ (26,174)	$ (5,669)	$ 9,698	$ 1,606	$ 44,625
	Task 3	$ 21,988	$ 4,777	$ 18,574	$ (3,884)	$ (4,536)	$ 7,758	$ 1,285	$ 35,700
	Task 4	$ 4,050	$ (12,546)	$ 758	$ (20,898)	$ (4,374)	$ 7,481	$ 1,239	$ 34,425
	Task 5	$ -	$ -	$ -	$ -	$ -	$ -	$ -	$ -
	Task 6	$ -	$ -	$ -	$ -	$ -	$ -	$ -	$ -
Non-Federal Share		$ -	$ -	$ -	$ -	$ -	$ -	$ -	$ -
Total Variance - Quarterly (Federal and Non-Federal)		$ -	$ -	$ -	$ -	$ -	$ -	$ -	$ -
Cumulative Variance		$ 52,503	$ 25,637	$ 48,044	$ (9,755)	$ (25,953)	$ 1,755	$ 6,343	$ 133,843

13. COLLABORATIVE LEVERAGING.

We are currently collaborating with 1 Ph.D. student in the Zoback research group at Stanford University. Additional, collaboration is ongoing with the Hakala and Lopano groups at NETL. A new LDRD proposal has been submitted that would support the development of machine learning algorithms for accelerating segmentation of synchrotron μ-CT image data. If successful, this activity will strongly support the existing NETL project.

14. CONCLUSIONS

The manuscript for Task 2 has been completed and submitted for review in Energy & Fuels. A total of 3 peer-reviewed extended manuscripts (conference papers) for the 2018 URTeC have been published. The kerogen manuscript submitted to Energy & Fuels was reviewed and a new version of the manuscript comments was submitted and is awaiting a final decision from the editor on publication. We submitted a new FWP for the project to DOE-HQ outlining our plans for extension of our project. Additionally, we have started a new industrial collaboration with Pioneer Natural Resources to understand mineral scaling problems in the Permian Basin.

The properties of the altered zone at shale surfaces are centrally important to developing chemical manipulation technologies by which shale interfaces can be controlled *in-formation* to increase access to matrix. In this quarter, we presented important new results that help to constrain two seminal properties of the altered zone: *thickness* and *permeability*. Image segmentation analysis of μ-CT data of post reaction cores for both Marcellus-PA and Eagle Ford show the depth of penetration of the fracture fluid into the shale matrix altered zone to be *ca* 1 mm. Microfractures were important foci of shale alteration in both Marcellus and Eagle Ford shales.

In our Quarter 6 report, we showed that Marcellus shale permeability decreased 20% after reaction with fracture fluids, whereas Eagle Ford porosity increased by an order of magnitude. However, we did not present microscale results that could explain this sharply contrasting behavior. In the present report, we show that the bulk density of the reacted Marcellus shale increased, implying that porosity was destroyed or disconnected. In contrast, in Eagle Ford shale, we showed that porosity increased by over 4%, indicating the porosity-generation out-stripped the negative impacts of barite precipitation. These findings provide an explanation for the previously reported permeability changes and provide valuable insights for designing manipulation strategies.

In Task 3&4(c), a chemical model was built for our previous shale "sand" experiments conducted in 2016 and 2017 to *(1)* refine the kinetic rate constant for bitumen-catalyzed Fe(II) oxidation and to *(2)* better understand the chemical reaction mechanisms during shale-fluid interactions. The modeling results reproduced the experimental data with the rate constant for bitumen-catalyzed Fe(II)-oxidation reaction tuned to be 8×10^5 mol/kg/yr for Marcellus and 8×10^7 mol/kg/yr for Eagle Ford. This reaction pathway is shown to be critical for both Marcellus and Eagle Ford systems in capturing Fe(II) oxidation trends measured in the experiments. Modeling results also suggest that pyrite dissolution is limited by accessibility of fracture fluid to pyrite grains inside the sand particles. In addition, the dissolved O_2 in the initial fracture fluid can be quickly consumed by pyrite dissolution, and further dissolution of pyrite and Fe(II) oxidation require continuous supply of O_2 from the headspace of the reactor, or in real subsurface hydraulic fracturing sites, from continuous injection of fracturing fluid from surface.

APPENDIX A. Deliverables

Publications.

URTeC Extended Abstracts (2018)-

1. Barium Sources in Hydraulic Fracturing Systems and Chemical Controls on its Release into Solution. Adam D. Jew, Qingyun Li, David Cercone, Kate Maher, Gordon E. Brown, Jr., John R. Bargar

2. Imaging Pyrite Oxidation and Barite Precipitation in Gas and Oil Shales. Qingyun Li, Adam D. Jew, Andrew M. Kiss, Arjun Kohli, Abdulgader Alalli, Anthony R. Kovscek, Mark D. Zoback, David Cercone, Katharine Maher, Gordon E. Brown, Jr., John R. Bargar

3. Effects of hydraulic fracturing fluid on shale matrix permeability. Abdulgader Alalli, Qingyun Li, Adam Jew, Arjun Kholi, John R. Bargar, Mark Zoback

Energy & Fuels (In Review)-

4. Shale Kerogen-Hydraulic Fracturing Fluid Interactions and Contaminant Release. Megan K. Dustin, Adam D. Jew, Anna L. Harrison, Claresta Joe-Wong, Dana L. Thomas, Katharine Maher, Gordon E. Brown, Jr., John R. Bargar

5. Organic and Inorganic Controls on Barite Precipitation in Hydraulic Fracturing Systems. Adam D. Jew, Qingyun Li, Kate Maher, Gordon E. Brown, Jr., John R. Bargar

Environmental Science & Technology (In Preparation)-

6. The Effect of Hydraulic Fracturing Fluid on the Stability of Uranium in Unconventional Oil/Gas Shales. Adam D. Jew, Clemence J. Besancon, Scott J. Roycroft, Vincent S. Noel, Gordon E. Brown, Jr., John R. Bargar

Presentations at National Meetings.

7. AIChE Annual Meeting, Oct. 29-Nov. 3, 2017, Minneapolis, MN. Adam D. Jew, David Cercone, Qingyun Li, Megan K. Dustin, Anna L. Harrison, Claresta Joe-Wong, Dana L. Thomas, Kate Maher, Gordon E. Brown, Jr., John R. Bargar. *Chemical controls on secondary mineral precipitation of Fe and Ba in hydraulic fracturing systems.*

8. AGU Fall Meeting, Dec. 11-15, 2017, New Orleans, LA. Qingyun Li, Adam D. Jew, Gordon E. Brown, Jr., John R. Bargar. *Chemical reactivity of shale matrixes and the effects of barite scale formation*

9. DOE Upstream Workshop, Feb. 14, 2018, Houston, TX. Alexandra Hakala, Joe Morris, John Bargar, Jens Birkholzer. *Fundamental Shale Interactions-DOE National Laboratory Research*

URTeC Conference, July 23-25, 2018, Houston, TX:

9. Adam D. Jew, Qingyun Li, David Cercone, Kate Maher, Gordon E. Brown, Jr., John R. Bargar. *Barium Sources in Hydraulic Fracturing Systems and Chemical Controls on its Release into Solution*.
10. Qingyun Li, Adam D. Jew, Andrew M. Kiss, Arjun Kohli, Abdulgader Alalli, Anthony R. Kovscek, Mark D. Zoback, David Cercone, Katharine Maher, Gordon E. Brown, Jr., John R. Bargar. *Imaging Pyrite Oxidation and Barite Precipitation in Gas and Oil Shales*
11. Abdulgader Alalli, Qingyun Li, Adam Jew, Arjun Kholi, John R. Bargar, Mark Zoback. *Effects of hydraulic fracturing fluid on shale matrix permeability*.

Other activities.

- Participant in DOE-FE Oil and Natural Gas Knowledge Management adviser group (A. Jew)
- Participant in DOE-FE Oil and Natural Gas Science Leadership adviser group (J. Bargar)